

**Department of Physics and Astronomy
University of Heidelberg**

Bachelor Thesis in Physics
submitted by

Lukas Röhrich

April 2021

External Coupling and Modifications to an Ultra-Fast Laser Pulse Setup to Allow Higher Infrared Peak Intensities

This Bachelor Thesis has been carried out by Lukas Röhrich at the
Max-Planck-Institute in Heidelberg
under the supervision of
Prof. Dr. Thomas Pfeifer
and
Priv.-Doz. Dr. Robert Moshhammer

External Coupling and Modifications to an Ultra-Fast Laser Pulse Setup to Allow Higher Infrared Peak Intensities - In this thesis, a modification of an experimental setup, able to analyse atom dynamics during interaction with a high intensity field, and the first steps towards implementation are presented. The idea of the experiment is to utilize high intensity infrared (IR) radiation to perturb the atom's potential, while exciting or ionizing them with extreme ultra violet photons. The planned modifications are: 1) an external coupling of one part of the IR pulse into the existing experiment, which consists of a time delay stage and an off-axis parabolic Mirror and 2) using a high intensity IR Titanium Sapphire laser pulse centered about 800 nm, which will replace optical parametric amplified pulses centered around 1 to 2 μm . This leads to a more intense IR with a possible peak intensity in the regime of 10^{17} Wcm^{-2} . These technical modifications allow for a stronger perturbation of the benchmark atom Helium, for the purpose of investigating correlated two electron wavepackets in double ionization or excitation processes.

Externe Einkopplung und Modifikationen für einen ultraschnellen Laserpuls-Aufbau zur Ermöglichung von Höheren Infrarot Spitzenintensitäten - In dieser Arbeit werden eine Modifikation eines Versuchsaufbaus, der die Atomdynamik während der Wechselwirkung mit einem Feld hoher Intensität analysieren kann, und die ersten Schritte zu dessen Umsetzung vorgestellt. Die Idee des Experiments ist es, hochintensive infrarote (IR) Strahlung zu nutzen, um das Potential der Atome zu stören, während sie mit extrem ultravioletten Photonen angeregt oder ionisiert werden. Die geplanten Modifikationen sind: 1) eine externe Einkopplung eines Teils des IR Pulses in das bestehende Experiment, welche aus einer Zeitverzögerungsstufe und einem Off-Axis-Parabolspiegel besteht, und 2) die Verwendung eines hochintensiven IR Titan-Saphir Laserpulses, der bei etwa 800 nm zentriert ist und optisch-parametrisch verstärkte Pulse im Bereich von 1 bis 2 μm ersetzen wird. Dies führt zu einem intensiveren IR Feld mit Spitzenintensitäten im Bereich von 10^{17} Wcm^{-2} . Diese technischen Modifikationen erlauben eine stärkere Störung des Referenzatoms Helium, um korrelierte Zwei-Elektronen-Wellenpakete bei Doppelsonisations- oder Anregungsprozessen zu untersuchen.

Contents

1	Introduction	5
2	Theory	7
2.1	Ultra-Short Pulses	7
2.2	High Harmonic Generation	9
2.3	The Helium Atom	12
2.4	Off-Axis Parabolic Mirror	15
2.5	Absorption Spectroscopy	17
3	Experimental Setup	19
3.1	Laser System - Ultra-Short Pulse Generation	19
3.2	Modifications to the Laser System	21
3.3	Beamline - HHG and Measurement	23
3.4	Modifications to the Beamline	25
3.5	Intensity Estimation	27
4	Conclusion	31
	Glossary	33
	References	34
	Appendix	36
	Acknowledgment	41

1 Introduction

Light and matter surround us and are presently two of the most examined physical phenomena. Matter makes up everything from the ground you are standing on, the air you are breathing to the screen you are looking at and all the materials used to manufacture it. All the technologies, that humans have invented and use are made out of tiny, massive building blocks called atoms. Some of these technologies, for example computers or medical instruments, are already at the threshold of using physical phenomena on the atomic scale. Hence, understanding the properties of atoms helps us to create even better technologies. Light is as pervasive as matter and drives the fundamental phenomena in nature on both the large scale, in nourishing the evolution of life with energy, as well as on the small scale, like in the excitation of atoms.

Discoveries like the photoelectric effect in the late 19th century made it clear that the behaviour of matter can be altered with light [1]. Since then, many inventions based on these light-matter interactions, such as the laser, have pushed forward the technical limits to which humanity has reached. However, we are still not able to fully describe the dynamics within an atom completely, but since the scientific revolution, dating back to several centuries ago, the direction of marching is set. The description of observations in nature and the falsification of hypotheses by empirical evidence will eventually answer our questions.

The interaction of light with matter can be altered by excitation and further perturbation with energetically matching, right-timed pulses of light. The *Quantum Dynamics Control Group* at the *Max Planck Institute for Nuclear Physics* in Heidelberg, Germany provides an experimental setup, which is able to perform ultra-fast light interaction with gaseous media. This is done by the generation of ultra-fast laser pulses (femtoseconds [*fs*] to attoseconds [*as*]) in the regime of *InfraRed* light (IR; 780 nm - 1 μ m) inducing *High Harmonic Generation* (HHG), which converts a part of the IR light into *eXtrem Ultra Violet* (XUV; 10-200 nm) laser pulses. Both light pulses, IR and XUV, interact with the target medium to be studied, triggering dynamical processes within the atoms, which are observed using absorption spectroscopy.

As helium, with its rather light nucleus and two electrons, is the second easiest atom existing and the most easiest atom not solvable analytically, it is often used as a benchmark-atom to evaluate the performance of techniques. Hence, its investigation is of great interest within the field. Most excitation transitions of helium from the ground state or the direct ionization of one or both electrons are within the XUV regime. Both electrons can be excited with a single photon which is called *double excitation*. This leads to Rydberg series of excited states distinguished by the number of the main shell *N* of the inner, energetically lower

lying electron. Within one series, both electrons are able to take a variety of states with rising energy levels up to the ionization of the outer electron, which is called *single ionization*, or even both, in the process of *double ionization*. Depending on the actual dynamics within the atom, its light absorbance and emittance varies, which can be manipulated externally with light pulses within the IR regime as for example demonstrated in [2].

Recent work, like [3], helped understanding the dynamics of the XUV excited and IR perturbed helium atom below the $N=2$ threshold. The goal of this thesis project are several modifications to the existing experiment, which clear the field to achieve stronger perturbation of the helium atom, e.g. measurable at the double ionization process or higher lying $N \geq 3$ Rydberg series with higher electron correlation. These modifications are therefore a contribution to gain a better understanding of the interaction of light with correlated electron systems based on the two electron correlation in helium. The goal is to reach a strong IR laser field, which is able to manipulate the electron dynamics of helium to a higher extent. This is achieved by the design and implementation of technical modifications, which will enhance the peak intensity of the focused IR pulse interacting with the helium atoms. For this, the following properties of the IR beam need to be optimized: the pulse energy, the pulse duration and the focal spot size. Hence, the laser generating system was modified and the experimental setup was complemented by an additional beam-path for a part of the IR pulse, which makes it possible to unlock higher peak intensity regimes for perturbing the atomic potential.

In this thesis these modifications are presented combined with the underlying theoretical background. It is thus structured as follows: introduced in Chapter 2 is the physical theory which is necessary to understand the phenomena used within the experimental setup. It starts with a description of *Ultra-Short Pulses* in Chapter 2.1, followed by *High Harmonic Generation* in Chapter 2.2. In Chapter 2.3 a quantum mechanical view on *the Helium Atom* is elaborated after which the *Off-Axis Parabolic Mirror* in Chapter 2.4 and the *Absorption Spectroscopy* in Chapter 2.5 is described. Following in Chapter 3, the experimental setup and the modifications partly implemented, partly planned are presented. This Chapter is subdivided in the explanation of the *Laser System* in Chapter 3.1, followed by the applied *Modifications to the Laser System* in Chapter 3.2. In Chapter 3.3 the experiment's *Beamline* is explained as well as *the Planned Modifications* to this part of the setup in Chapter 3.4. Lastly, in Chapter 4 a conclusion as well as an outlook for further improvements to the experiment are given.

2 Theory

This chapter provides the theory for this thesis. Given are qualitative descriptions and the mathematics to understand the physical concepts used. The order of the sub chapters follows the order in which their topics are used in the experimental setup (see Chapter 3) from start to finish.

First is the description of *Ultra-Short Pulses* of light in Chapter 2.1 which are key for measuring ultra-fast processes. Chapter 2.2 explains *High Harmonic Generation* which is used to generate XUV pulses. A quantum mechanical description of the target medium *Helium* is given in Chapter 2.3. Also given is an overview of the states below the $N=3$ threshold, which can be reached with the given modifications of the experimental setup, as well as some double ionization thresholds. The key component of the planned external coupling is the *Off Axis Parabolic Mirror*, which geometry is explained in Chapter 2.4. At last, Chapter 2.5 gives a theoretical understanding of *Absorption Spectroscopy*, which provides the signal measured at the end of the setup.

2.1 Ultra-Short Pulses

When ultra-short pulses are mentioned in recent literature it is often in reference to pulses with a duration of *fs* to *as* (in numbers: $10^{-15} - 10^{-18}s$). This chapter will give an understanding on how to describe these pulses reasonable and follows mainly the argumentation of [4].

A simple, but in practice not common example for a pulsed laser beam propagating along the Z -axis is a *Gaussian Pulse*

$$\vec{E}(x, y, z, t) = \vec{E}_0 \exp \left[- \left(\frac{t}{\tau} \right)^2 \right] \exp \left[- \left(\frac{x^2 + y^2}{w^2} \right) \right] \exp \left[- i (kz - \omega t) \right] \quad (2.1)$$

\vec{E}_0 : amplitude of electric field, w : spatial pulse width,
 τ : temporal pulse width

which is depicted in Figure 2.1. For further examination the spatial part is neglected which reduces (2.1) to $E(t)$. This is a good example to study the temporal and spectroscopic properties of a short pulse.

Connected to the temporal field $E(t)$ is the spectrum of the field strength $\tilde{E}(\omega)$ via the Fourier transform \mathcal{F}

$$\begin{aligned}\tilde{E}(\omega) &= \mathcal{F}[E(t)] = \int_{-\infty}^{\infty} E(t)e^{-i\omega t} dt , \\ E(t) &= \mathcal{F}^{-1}[\tilde{E}(\omega)] = \frac{1}{2\pi} \int_{-\infty}^{\infty} \tilde{E}(\omega)e^{i\omega t} d\omega .\end{aligned}\tag{2.2}$$

It is convenient to define $\tilde{E}(\omega)$ to vanish for $\omega < 0$ as negative frequency provide no physical interpretation. The wave nature of electromagnetic fields motivates the representation of $E(t)$ by a product of an amplitude and a phase function

$$E(t) = \hat{E}(t)e^{i\Phi(t)} .\tag{2.3}$$

$\hat{E}(t)$: field envelope, $\Phi(t)$: phase

The temporal derivative of $\Phi(t)$ is the frequency $\omega(t)$ of the electric field. For the purpose of describing short pulses, which are in fact a superposition of frequencies within the interval $\Delta\omega$ rather than only one central frequency ω_c , it is useful to split the frequency in these two parts

$$\frac{d\Phi(t)}{dt} = \omega(t) = \omega_c + \Delta\omega(t) .\tag{2.4}$$

We can see from (2.4) that $\Delta\omega(t)$ contains time-dependent frequency components, which implies that different frequencies of the pulse spectrum can arrive at

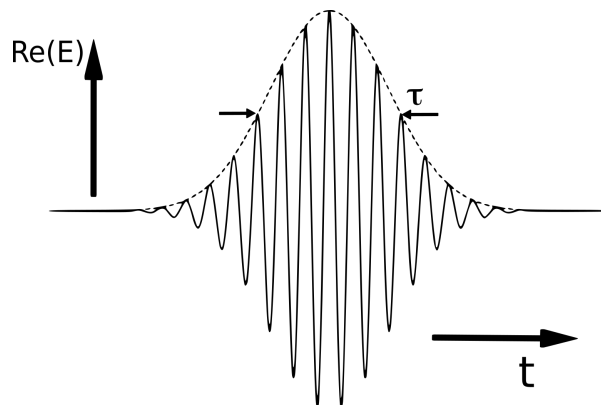


Figure 2.1: Example for a *Gauss Pulse*. τ gives the width of the pulse. The dotted line is the Gaussian envelope.

different times. If $\Delta\omega(t) \neq \text{const.}$ the pulse is said to be *chirped*. Similar to (2.3) its Fourier transform can be written as

$$\tilde{E}(\omega) = \hat{E}(\omega)e^{i\tilde{\Phi}(\omega)} . \quad (2.5)$$

The interaction of the spectral phase $\tilde{\Phi}(\omega)$ of a pulse with the medium it is propagating through yields interesting physics, which will help to understand processes ongoing in the experiment. Its Taylor-expansion of $\tilde{\Phi}$ up to the third polynomial reads

$$\begin{aligned} T_3\tilde{\Phi}(\omega; \omega_0) &= \sum_{n=0}^3 \frac{\tilde{\Phi}^{(n)}(\omega_0)}{n!} (\omega - \omega_0)^n \\ &= \phi_{CEP} + \phi_{GD} \cdot (\omega - \omega_0) + \phi_{GDD} \cdot (\omega - \omega_0)^2 + \phi_{TOD} \cdot (\omega - \omega_0)^3 . \end{aligned} \quad (2.6)$$

These derived quantities influence the behaviour of the spectral phase and therefore of the pulse itself. They are briefly described in the following: ϕ_{CEP} is the *Carrier Envelope Phase* which gives information about the temporal difference between the electric field maximum to the maximum of the pulse envelope. ϕ_{GD} represents the *Group Delay* which is a time delay given in [s] and tells by how much the whole pulse is shifted due to the influence of the medium the pulse is propagating through. The further components ϕ_{GDD} and ϕ_{TOD} are only non-zero if $\Delta\omega(t) \neq \text{const.}$ and give information about the chirp of the pulse. ϕ_{GDD} (*Group Delay Dispersion*, given in [s²]) thereby provides a linear chirp, ϕ_{TOD} (*Third Order Dispersion*, given in [s³]) a quadratic chirp.

It should be mentioned that higher order phase terms like ϕ_{GDD} and ϕ_{TOD} influence the pulse duration and intensity and can be observable depending on the medium the pulse is propagating through, as well as its wavelength. These factors are positive for most optical materials within common wavelength regimes, which elongates the pulse duration in time.

2.2 High Harmonic Generation

As the goal of this experiment is to excite and ionize helium atoms, XUV photons provide a well suited photon energy region as these match the transition energies for transitions from the ground to excited states. Also important for observing ultra-fast electron dynamics are pulses shorter than the lifetime of the excited states, which are in the few *fs* to *as* regime. Both properties can be reached by *High Harmonic Generation* (HHG), which will be further examined in this chapter

by providing a semi-classical approach of the *three-step model*.

The Coulomb potential of an atom can be perturbed by an intense electromagnetic field due to the *strong field interaction*. This will not be discussed in detail here and for further discussion, only the case of a potential applied by the strong laser field for rather low frequency and high intensity is examined. An example for this interaction is the *strong field ionization* shown in Figure 2.2. In Figure 2.2.a an unperturbed Coulomb potential of an atom is shown. The electron e^- is the energetically highest excited and thus outer most electron of the atom in its ground state. The dashed line represents the *ionization potential* I_P which is the energy required to ionize one electron of the atom. In Figure 2.2.b a strong electromagnetic field is applied to the atom. Its potential perturbs the Coulomb potential if the wavelength of the electromagnetic field is much larger than the size of the atom. Otherwise the change of the field would happen too fast to affect the atomic potential. This perturbation allows the electron to tunnel out of the atom leaving it ionized. Tunneling is a quantum mechanical process which is one of the reasons why the three-step model is semi-classical rather than completely classical. It follows a brief explanation of the three-step model. More detailed explanations of this model can be found in the pioneering works [5,6].

Given an electromagnetic field with the frequency ω_E and the period T_E , the strong field ionization represents the first step of the three-step model as shown in

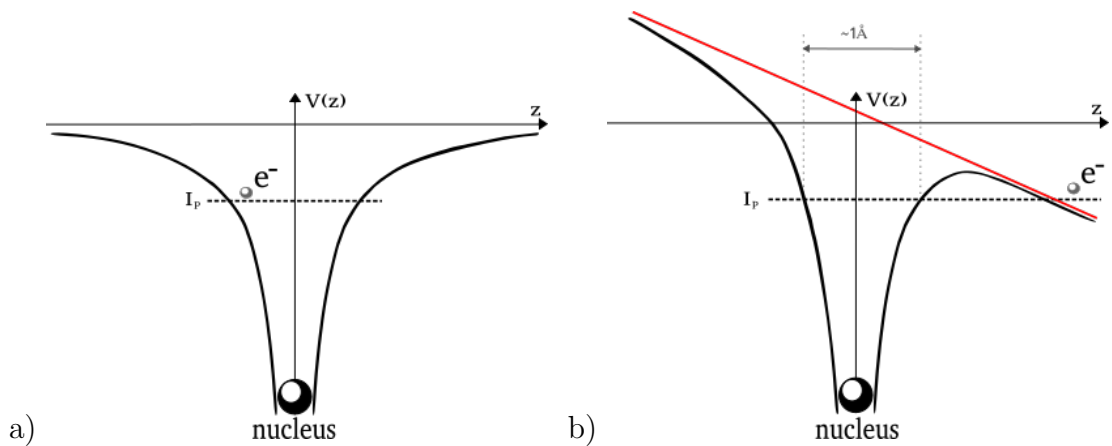


Figure 2.2: Schematic depiction of the *strong field ionization*. a) Electron in the unperturbed Coulomb potential (solid black line) of a nucleus. b) The slow varying potential of laser field (red) seems quasi-statically and affects the Coulomb potential. If strong enough, an electron is able to tunnel out of the atom.

Figure 2.3.a. In the second step the electron leaves the atom and interacts with the electromagnetic field which first accelerates it for a half of a period away from the atom. As the field reaches its extreme, in the depicted example a minimum, the field potential switches sign which causes a pull back of the electron and its acceleration back to the atom. For roughly another quarter of a period the velocity of the electron increases, giving it a rise in kinetic energy $E_{e^-}^{kin}$, which peaks around three quarters of a period after the initial step. The third step of the model is the recombination of the electron with the nucleus as it reaches its vicinity. This recombination releases energy in form of the emission of a photon with the frequency ω_{HHG} as shown in Figure 2.3.b. It may be important to note that the recombination does not take place only exactly after three quarters of a period after the starting of the process. Hence, the actual kinetic energy of the electron varies for each individual process. Therefore the frequency ω_{HHG} varies, because the released energy depends on the kinetic energy with

$$\hbar\omega_{HHG} = E_{e^-}^{kin} + I_P . \quad (2.7)$$

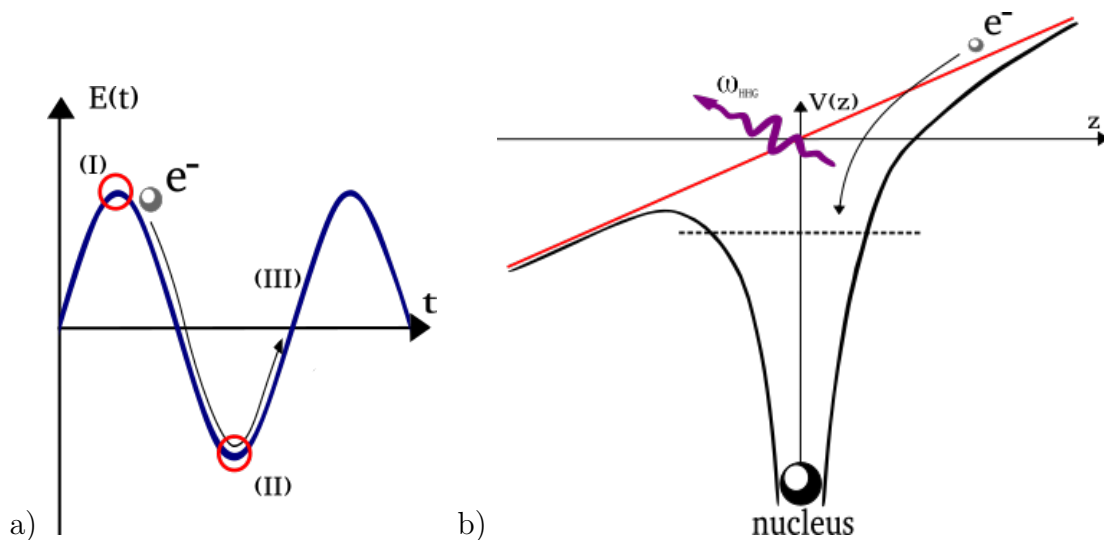


Figure 2.3: a) Overview of the *three-step model* shown for the field strength: (I) Ionisation of the electron; (II) Acceleration of the electron; (III) Recombination with the nucleus. See body text for description. b) Recombination step with photon emission. This step (III) most likely takes place during the second half of a period after the initial step (I) with the highest probability being $3/4$ of the period after the ionization, as marked in a).

The electron even is able to pass the nucleus several times before recombining [6]. The recombination is most likely with striking distance of the nucleus, which happens around the sign switches of the field $E(t)$.

As the initial process of the three-step model is most likely to be initiated for the highest electric fields strength and thus most steep rising/falling field potential, the release of HHG-photons occurs with a periodicity of $T_E/2$. This leads to a pulse train with a $T_E/2$ spacing in temporal domain and $2\omega_E$ spacing in spectral domain.

2.3 The Helium Atom

Helium with its two electrons around a rather simple nucleus is one of the most straightforward atoms existing, only excelled by hydrogen, which is the only atom for which an analytical description exists. It can be described with a quantum mechanical approach. This is widely done using the *Schrödinger Equation* (SEQ), of which an introduction can be found in [7]. Its necessity comes from the wave nature of all particles and in particular of electrons in the vicinity of a nucleus. Several experiments in the early 20th century like the famous double slit experiment or the Stern-Gerlach-experiment motivated the quantum mechanical view on more and more disciplines in physics and the latter especially in atomic physics. This chapter introduces the basics of the quantum mechanical description of the helium atom and shows a representation of the atom states below the $N=3$ threshold as well as some double ionization thresholds.

A state $\Psi(\vec{x}, t)$ of a system in quantum mechanics is a solution of the SEQ for that specific system. The SEQ can be written as

$$i\hbar\partial_t\Psi(\vec{x}, t) = \hat{H}\Psi(\vec{x}, t) . \quad (2.8)$$

$$\begin{array}{ll} \hbar & : \quad \text{Plancks constant,} \\ \partial_t & : \quad \text{partial time derivative,} \end{array} \quad \begin{array}{ll} \Psi & : \quad \text{state of system,} \\ \hat{H} & : \quad \text{Hamilton-Operator} \end{array}$$

Its Hamilton-Operator contains the actual information about the energetic relations within the system, as it describes the kinetic and potential energies. It can be written in matrix form, which gives rise to its eigenvectors with corresponding eigenvalues E_N . If, for example, \hat{H} describes the system of an atom, these eigenvectors are the states which can be inhabited by the electrons. E_N gives the energy levels of these possible states, where E_0 is the ground state and E_N with $N \geq 1$ are the excited states. In general these states of the electrons are distinguished

using a set of numbers. These numbers describe a basis of quantum numbers, in which the state of the electron is encrypted. Commonly used are the single electron quantum numbers $\{Nlm\}$, which follow out of the solution of the SEQ for the hydrogen atom using spherical surface harmonic functions Y_l^m [7]. As suggested in [8], they will be referred to as *spherical quantum numbers* in the following.

Due to the Coulomb interaction of the two electrons within a helium atom, solving its SEQ is not possible analytically. The break of spatial symmetry due to the two electrons inhibits the separation of the total wave function Ψ_{He} into a radial part and an angular part, as it is done for solving (2.8) for hydrogen. The potential of the atom is not spherical anymore. To approximate a model which treats helium similar to hydrogen, this break of the spherical symmetry is neglected and the SEQ is solved for each electron individually. Furthermore, a shielding factor is introduced, which is interpreted as the shielding of the atomic potential the second electron "feels" due to the first electron [7]. This and similar approaches motivate the usage of spherical quantum numbers for helium and even more complicated atoms, even though they are only approximations. The ground state of helium given in spherical quantum numbers is $1s^2$.

The interaction of the electrons gains in weight, if higher and higher excitations of the atom are considered. Therefore, the spherical quantum numbers fail to describe the state of the excited atom more and more. As motivated in [9], a different set of quantum numbers are better suited for describing states of helium with the inner electron at $N \geq 3$. The commonly used set are the *parabolic quantum numbers* $n(K, T)_N$, which were first introduced in [10]. Sometimes they are referred to as *Stark quantum numbers*. The quantum numbers N and n describe the principle quantum number of the inner and outer electron respectively, whereas the quantum numbers K and T are describing their angular relation.

Atomic states are grouped in symmetry groups, which are denoted with the *Spectroscopic Notation* $^{2S+1}L^{o/e}$. L is the total angular momentum, which is given in letters rather than numbers (0=S, 1=P, 2=D, ...) and S is the spin quantum number. The indices o/e indicate odd or even parity of the states. As the transitions between states are treated in the dipole approximation within this thesis, single photon transitions are only possible for $\Delta L = \pm 1$ and a change of parity. Hence, the $^1P^o$ -group is of most interest as transitions from the ground state $1(0, 0)_1$, which is part of the $^1S^e$ -group, into this group are the only possible ones. These transitions are in the XUV regime, which usage within this experiment is explained in Chapter 3. Transitions from the $^1P^o$ -group to the groups in the same energetic range, $^1S^e$ and $^1D^e$, are also allowed in the dipole approximation with

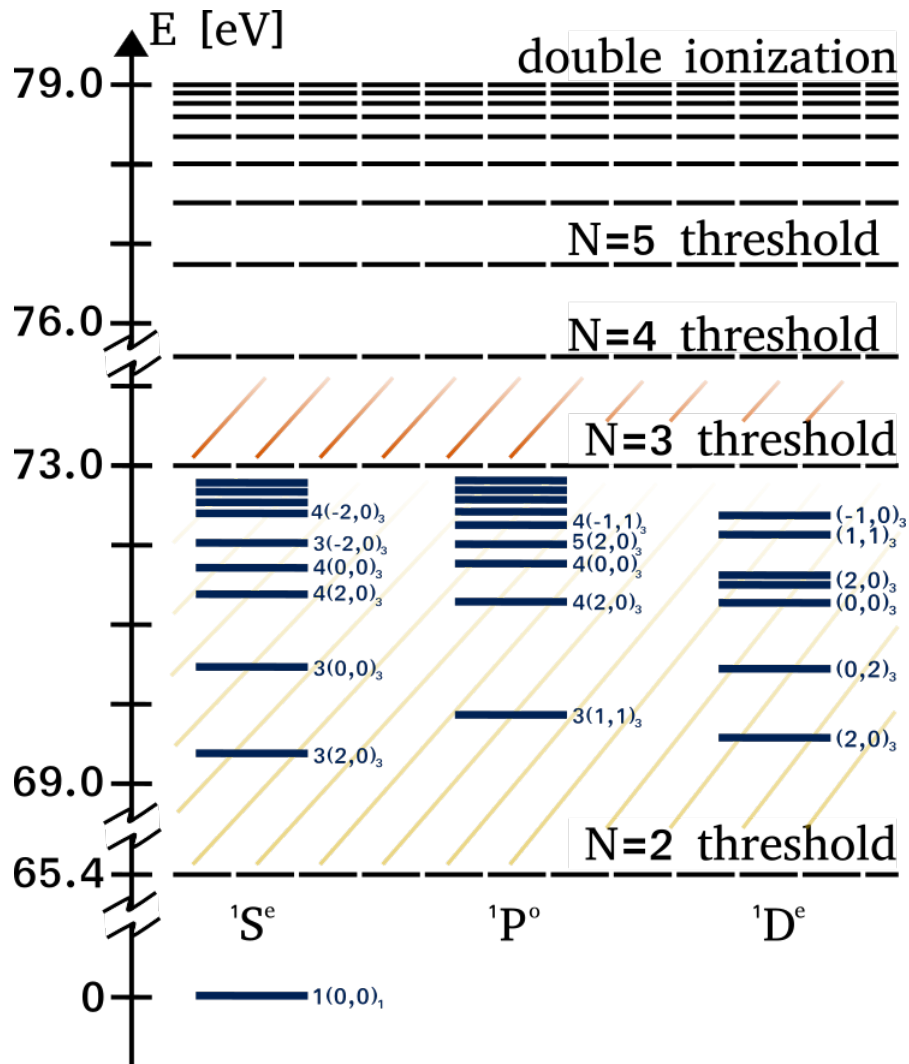


Figure 2.4: Doubly excited states of the helium atom given in *parabolic quantum numbers* $n(K, T)_N$ between the $N=2$ and $N=3$ threshold. The energy levels are obtained from [8, 11, 12].

the help of the low energetic IR photons.

All doubly excited states, for which the energetically lower lying electron has the same principal quantum number N , are gathered in Rydberg series. Within a series, excitation with more energetic photons leads to higher excited states, whereby the quantum numbers n , K and T differ. With higher and higher excitation energies the outer electron with its principal quantum number n will be removed to infinity eventually, which implies its ionization. The energetic limit at which the outer

electron is ionized while the inner electron still remains with a given quantum number N is called the N -*threshold*. If both quantum numbers N and n rise to infinity, *double ionization* is reached. Figure 2.4 shows an overview of states within these three groups for $N = 3$ given in the parabolic quantum numbers as well as several ionization thresholds. A more detailed table of helium states between the $N=2$ and $N=3$ threshold can be found in the appendix Chapter A.1. Given are their energy positions E in [eV] with the ground state $1(0,0)_1$ set to 0 eV and their line widths Γ in [eV]. The latter gives information about the lifetime τ of the excited state with

$$\Gamma \propto \frac{1}{\tau}.$$

2.4 Off-Axis Parabolic Mirror

One of the main goals of the modification of the experimental setup introduced in Chapter 3 is the reduction of the focal size of the IR pulse, as this provides a higher intensity at the target atoms, which are perturbed by the IR field. The focal size of the IR is connected to the focal length of the *Off Axis Parabolic mirrors* (OAP), which is described in the following, as well as an overview of the geometry of an OAP is given.

A parabolic mirror is a rotationally symmetric mirror surface the basic shape of which is a parabola. As depicted in Figure 2.5.a, each incoming ray, which

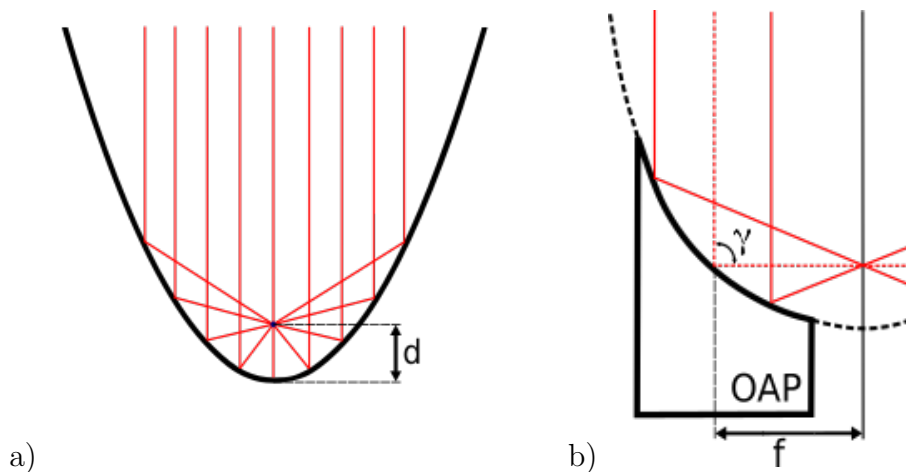


Figure 2.5: a) Parabolic mirror surface with the focal length d . b) OAP as a section of a paraboloid with the reflection angle γ and the focal distance f .

propagates perpendicular to the tangent at the origin of the parabola, is reflected to the same point with distance d to the origin. The length of d is determined by the function $p(x)$ which describes the underlying parabola :

$$p(x) = \frac{x^2}{4d} \quad (2.9)$$

[13] offers a geometric derivation of this relation. For an OAP only a slice of the parabola is used as shown in Figure 2.5.b, which gives rise to the effect that the collimated incoming beam is reflected by a given angle γ . This angle, as well as the focal distance f can be chosen by selecting the appropriate slice and varying d . In the case of this thesis project's modifications $f = 3'' = 76.2mm$ and $\gamma = 90^\circ$, as discussed later in Chapter 3.

Is introduced in [13] is the relation between the divergence angel θ of the beam and its minimal beam radius w_0 :

$$\tan \theta = \frac{\lambda}{\pi w_0} . \quad (2.10)$$

θ : divergence angel, λ : wavelength,
 w_0 : beam waist

Due to their reciprocal relation the beam waist shrinks with increasing angel of divergence. This is the reason why using a shorter focal length f scales down the spot size of the beam, as the shorter f implies a higher divergence.

To achieve this shorter focal length, OAPs are used as they provide several advantages within this experimental setup compared to other solutions as for example using lenses. These advantages are:

- 1) For focusing with lenses the pulse needs to propagate through the lens material, which gives rise to dispersion effects broadening the pulse in duration (see GDD and TOD in Chapter 2.1).
- 2) Chromatic aberration hampers the focusing to small spots, as the short IR pulse contains a broad spectrum of wavelengths.
- 3) Focusing into a given beampath can be achieved with a single OAP, whereas at least one mirror and one lens would be needed to have the same result. Therefore, an OAP is more space saving.

Mainly disadvantageous when using an OAP is, that all of its 6 degrees of freedom (3 in translation, 3 in rotation) are altering the focal behaviour.

2.5 Absorption Spectroscopy

As this thesis' experiment is interested in light-matter interaction on an atomic scale, it is crucial to quantify how light is affected by the atoms. One way of doing so is with *Absorption Spectroscopy* (AS), which yields insights into the electron dynamics of the utilized atoms by measuring the out coming light spectrum. This chapter will introduce the basic concept of AS.

Every object, which is made of atoms, absorbs and emits light. This is the reason most objects have colour and can be seen with the human eye. Which wavelengths of light - so to speak which colours - are absorbed and which are emitted depends on the atoms and molecules the object is made of. Every atom has its own characteristics when it comes to the interaction with light. A commonly used property of quantifying these characteristics is the *Optical Density* (OD)

$$OD(\omega) := \log_{10} \left(\frac{I(\omega)}{I_0(\omega)} \right) = \frac{\sigma(\omega)}{\ln(10)} \rho l , \quad (2.11)$$

ρ : density of medium, l : length of medium in propagation
 $\sigma(\omega)$: absorption cross section

which expresses the ratio between the intensities of the incoming light $I_0(\omega)$ and the outgoing spectrum $I(\omega)$. Because of the division only the atom response is observed, as the out coming spectrum still contains unaffected components of the incoming spectrum. OD can also be expressed with the absorption cross section σ . As the atoms are getting excited by the photons, the dipole moment $d(\omega)$ of these atoms changes as well. The dipole moment is simply the product of the charge and the displacement vector from the negative to the positive charge, that is, from the electron to the nucleus. It is connected to the macroscopic polarization P of the whole object via the atomic number density. The relation of $\sigma(\omega)$ to $d(\omega)$ is

$$\sigma(\omega) = \frac{\omega}{c\varepsilon_0} \operatorname{Im} \left[\frac{d(\omega)}{\tilde{E}(\omega)} \right] . \quad (2.12)$$

c : speed of light, ε_0 : electric permittivity in vacuum
 $d(\omega)$: dipole response, $\tilde{E}(\omega)$: electric field

Its derivation can be found in [14]. This relation can be interpreted as an interference of the incoming light with the outgoing light.

3 Experimental Setup

For measuring dynamical processes which take place in a temporal regime of ultra-fast physics, it is necessary to have an experimental setup which is able to resolve these processes fast enough. This fast resolution is achieved by the generation of ultra-fast IR pulses, whose spectrum is shifted into an XUV regime in order to excite or ionize the target atom helium. The experimental setup used for this thesis is elaborated in this chapter, reduced to the essential parts to provide an explanation of the underlying principles. Several thesis projects improved its performance over the last couple of years. From the installation of the laser system, including a three step amplification chain and an *Optical Parametric Amplifier* (OPA) [3] and the installation of the beamline [15–17], to the most recent modification, which is the installation of a *Hollow Core Fiber* (HCF) [18]. The combination of the OPA and HCF allow intense and stable performance whilst the central frequency of the produced IR light can be varied, which causes a loss in terms of intensity. Therefore, in this thesis project, only a 800nm beam is used for increased pulse energy. These modifications were applied at the first part of the setup - the *Laser System*. To increase the range of attainable experiments, modifications are as well applied on the second part of the setup - the *Beamline*. The following chapter discusses the Laser System in Chapter 3.1 and the Beamline in Chapter 3.3 and necessary modifications to these parts in Chapter 3.2 and Chapter 3.4, respectively. The modifications are the coupling of the LE in the HCF, the optimization of the LE compression and the installation of the external coupling at the beamline. These influence the beam energy, the pulse duration as well as the focus size, which will lead to an estimation of a lower limit for the peak intensity possible at the IR focus in the target medium.

3.1 Laser System - Ultra-Short Pulse Generation

Central for the generation of ultra-short laser pulses used in this experimental setup is a commercial system constituted of several components: a *titanium sapphire oscillator*, a *regenerative amplifier* (regen), *conventionally* and *cryogenic cooled Single Pass Amplifiers* (SPA and cryo SPA) and a *High Energy Optical Parametric Amplifier for Titanium Sapphire lasers* (HE-TOPAS). The regen, the SPA and the cryo SPA together with one initial stretcher and two grating compressors make up the *Chirped Pulse Amplifier* (CPA). Figure 3.1 shows an overview of the components which will be discussed in the following.

The pulse generation starts at the oscillator where a titanium sapphire crystal is pumped optically. With the help of Kerr-lensing [4] fs-pulses are already gained in this initial process with a central frequency at ~ 800 nm. These pulses

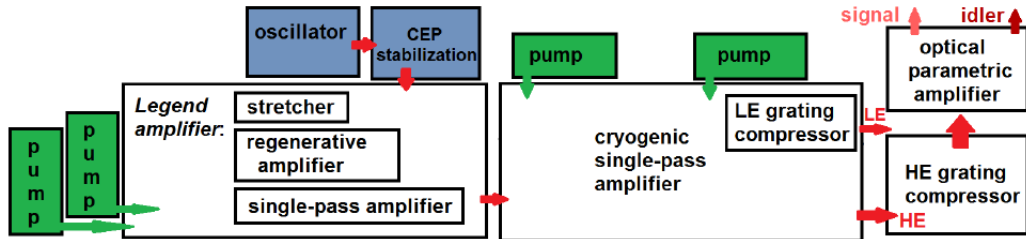


Figure 3.1: Simplified illustration of the laser amplification chain. The laser pulses are initially generated at the oscillator (blue). The pump lasers (green) provide energy to pump the amplifier crystals. After stretching the pulses in time, their intensity is increased. LE and HE are again compressed in time. The HE is shifted in frequency by the optical parametric amplifier. Image adapted from [3].

are amplified with three different sequential amplification stages. First up is the stretcher which broadens the pulse in time up to 150 ps by using the chirp explained in Chapter 2.1. These longer pulses have a much lower intensity due to energy conservation which allows another titanium sapphire crystal to amplify the pulses without destroying the crystal itself or other optical elements. Further and final amplification is gained by a single pass through the SPA and the cryo SPA. After the pulse gained an energy of around 26 mJ, it is split with an adjustable half-wave plate into two distinct pulse beams - the so-called *High Energy* (HE) and *Low Energy* (LE) pulses. Both pulses are compressed to ultra-short pulses using compressors, each consisting of two gratings. During compression, the non-linear phase terms, Φ_{GDD} and Φ_{TOD} derived in Chapter 2.1, can be optimized whereby the pulses end up close to a linear phase-gradient throughout the pulse (Fourier transform limited pulse). The central wavelength of the HE pulse can be shifted using the HE-TOPAS, which is an OPA [19], and has been used further for the experiment up to now, while the TiSA LE pulse was just blocked and not utilized. The roles of the HE and the LE pulses will be swapped as elaborated in the following Chapter 3.2.

After exiting the HE-TOPAS, the pulses are of short temporal duration and high intensity. However, to shorten the pulses even more, a HCF was introduced to the system [18]. The HCF also provides an easy and inexpensive method to guide laser beams over long distances. The central idea for shortening the pulse is to use nonlinear *Self-Phase Modulation* (SPM) [20] for broadening the pulse spectrum. The OPA pulses can be compressed afterwards with thin glass plates, whereas the LE TiSa pulses, centered around 800 nm, would need a chirped mirrors setup.

Given that the previous setup only operated on OPA pulses, this was not needed and is thus not installed. Therefore the SPM in the HCF is not used for the LE pulses. After propagating through the HCF, the pulse enters the next major section of the experimental setup - the beamline.

3.2 Modifications to the Laser System

The laser system explained in Chapter 3.1 was modified in several ways to match the requirements of the new experimental setup. The modifications are the coupling of the LE beam into the HCF and its compression optimization after the HCF. The TiSa LE pulses are not passing through the OPA and thus stay at their central wavelength of 800nm. This chapter briefly presents these modifications as well as the pulse characteristics after its optimization.

After exiting the LE grating compressor (see Figure 3.1), the LE beam is

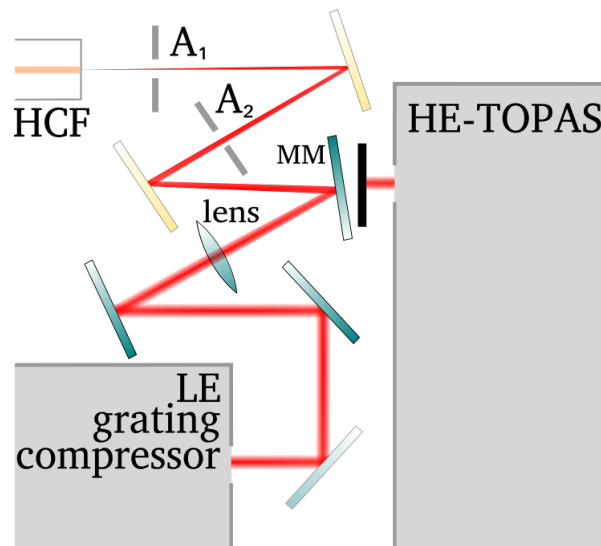


Figure 3.2: Modifications to couple the LE into the HCF. The non-greyled part is the optical modifications carried out within this thesis. The OPA pulse coming out of the HE-TOPAS is blocked and the LE is focused into the HCF with a $f = 3m$ lens. Apertures A_1 and A_2 are used to align the laser roughly. MM is a magnetic mirror which can be removed easily, allowing to use of the HE OPA beam. Dielectric (blue) are used for the 800 nm TiSa, whereas the gold mirrors (yellow) were designed for the HE-TOPAS, but are reused for the 800 nm because of high enough reflectivity at the given wavelength.

$\emptyset \sim 3\text{cm}$ in size ($\frac{1}{e^2}$). As suggested in [21], the optimal beam size a_{beam} for a given inner diameter a_{HCF} of the HCF is $a_{beam} = 0.65a_{HCF}$. As the used HCF has $a_{HCF} = 550 \mu\text{m}$, the collimated LE beam is narrowed down to $a_{beam} = 350 \mu\text{m}$ with a $f = 3 \text{ m}$ lens. This provides an optimal propagation through the HCF with a minimal power loss. Figure 3.2 schematically shows the optical setup after the grating compressor which couples the LE into the HCF.

Before the grating compressor, the pulse energy of the LE is $E_{uncompressed} = 9.89 \text{ mJ}$. After the compression, it lost about 27%, leaving it to 7.18 mJ, which is further reduced to 6.26 mJ right before the HCF entrance due to unavoidable clipping on, as well as absorption losses at the optical elements. Motivated by adjustment measurements, the power efficiency of the HCF is estimated to be $\sim 45\%$ which leads to an approximated power right after the HCF of $E_{HCF} = 2.82 \text{ mJ}$.

With the *Frequency Resolved Optical Gating* (FROG) setup introduced in [3], compressed fs pulses can be measured. In short, the FROG setup measures a spectrogram $S(\omega, t)$ which depends on the time delay t between the laser pulse to be measured and a non-linear grating function, which is generated by a part of the pulse itself. With an iterative algorithm, full temporal pulse information in form of the amplitude and phase is retrieved.

The LE compressor is used to minimize the chirp measured with the FROG closely before the beamline, to ensure that the pulses are temporally compressed at the experiment. Figure 3.3 shows the retrieved FROG data before and after the optimization. The time axis is centered at the maximum of the amplitude. Figure 3.3.a shows a chirped pulse, because the intensity distribution over time delay and frequency, the frequency spectrogram $S(\omega, t)$, is of diagonal shape. This leads to an elongation of the pulse in time as shown in Figure 3.3.b. Because the pulse is chirped, one can also see a quadratic behaviour of the phase within the main intensity peak of the pulse. Figure 3.3.d shows a close to linear phase during the main amplitude. Hence the chirp seems compressed very well. After the optimization some minor pulses before and after the main pulse, so-called pre- and post pulses, remain. This gives space for further improvement in the optimal compression of the LE pulse.

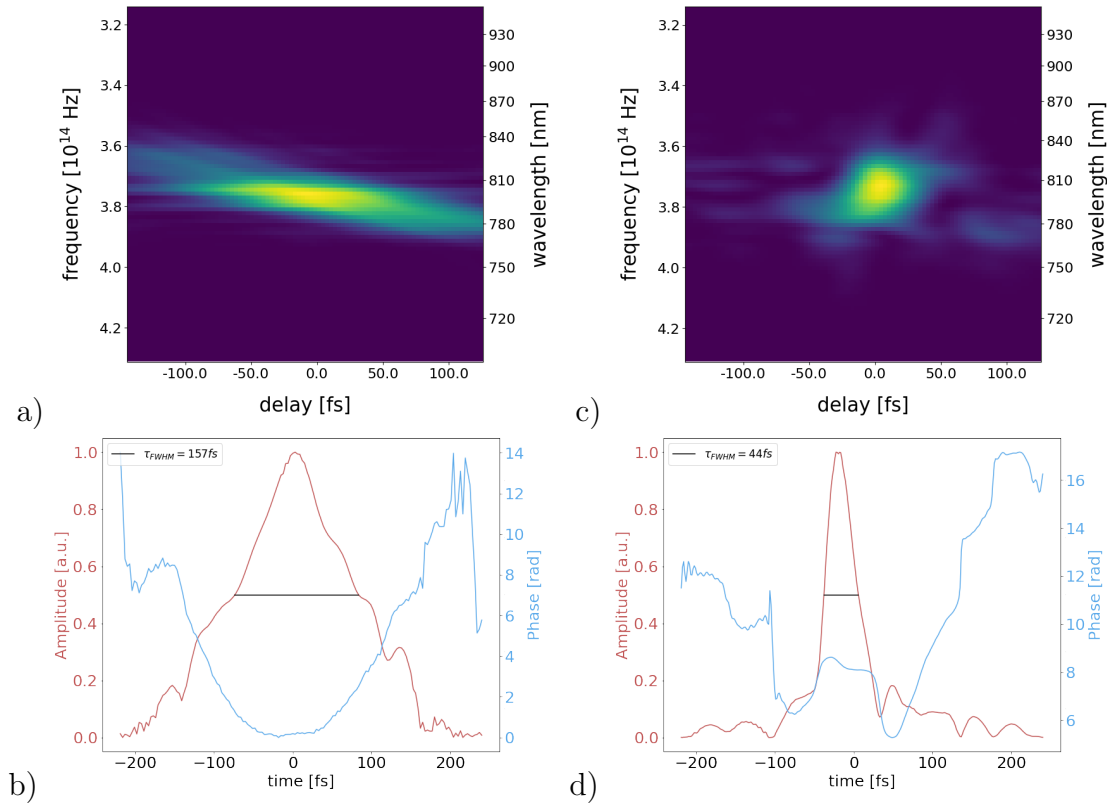


Figure 3.3: Retrieved FROG measurement before (a,b) and after (c,d) the optimization with the LE grating compressor. (a,c) show the 2D intensity depending on the frequency and the time delay of the interfered pulses - the spectrogram. (b,d) show the amplitude and the phase over time. Phase information at high amplitudes is more likely to be retrieved correctly than at low amplitudes. τ_{FWHM} is the pulse duration measured as *Full Width Half Maximum*.

3.3 Beamline - HHG and Measurement

With exiting the HCF the high-intense, ultra-short laser pulses also exit the clean-room environment of the setup and enter the experimental setup called beamline. This part of the experiment is designed to be mobile, which makes it usable with different laser sources. Presented in this chapter is the original setup without the modifications planned and conducted in this thesis project, with which reference measurements can be done to evaluate experimental improvements. An overview can be seen in Figure 3.4. The goal of the experimental setup is to measure XUV spectra of atoms or molecules perturbed by an ultra-short and intense IR pulse. To achieve this goal, the following steps are realized within the beamline: gener-

ation of XUV photons based on HHG, temporal and spatial variation of the IR and XUV beam, supply of a target medium in gaseous form and finally an XUV spectrometer measuring the target specific absorption. Because XUV photons can be reabsorbed in air, this part of the experiment needs to be placed in vacuum chambers.

After a few steps of laser alignment, the pulse is focused with a curved mirror and position corrected automatically with a stabilization system for steady coupling into the first vacuum chamber - the *HHG-chamber* at below 10^{-7} mbar or around 10^{-3} mbar (without and with HHG gas). This focusing and stabilization is shown in a simplified version in Figure 3.4. In the HHG-chamber a part of the IR pulse is converted into an XUV pulse using the HHG process (see Chapter 2.2) within the HHG cell, which is an exact copy of the target cell described below. The rest of the IR pulse propagates along the same axis as the XUV pulse, but with a greater divergence angle after the focus within the HHG cell, leaving the XUV photons mainly at the core of the mixed beam. Even though both pulses use the same path, their spatial extensiveness allows to separate the two, using a *zirkon Half Moon filter* (HM filter), whose horizontal edge is positioned off center as shown in the upper panel of Figure 3.4 to filter out the IR from the upper half leaving an XUV only beam, whereas the lower half becomes an IR only beam. This enables measurements of an IR intensity dependent XUV spectrum as well as a time-delay dependent XUV spectrum, where for the latter, the time delay is defined as the temporal difference between the IR and XUV pulse at the target cell.

This spatial and temporal separation takes place in the second vacuum chamber - the *mirror chamber* - at below 10^{-7} mbar gas pressure. It contains a toroidal (tor) and four motorized mirrors (M), of which only two are used for this experiment. The toroidal mirror has a rather large focal length of $1m$, which refocuses the beams into the target cell. As described in Chapter 2.4, this leads to a relatively large beam waist of the IR at the focus. So the remaining pulse energy of the IR is distributed over a large area at the focal plane, leading only to a medium high intensity. Gaining a higher peak IR intensity by shortening the focal distance is the main goal of this thesis project and will be introduced in the next chapter. The motorized split mirrors allow a control of the aforementioned time delay between the spatially separated IR and XUV pulse by a spatial offset and thus leading to different beam path lengths.

The next main vacuum chamber is the *target chamber*, also with a gas pressure below 10^{-7} mbar without target gas. Its main component is the target cell which is a hollow but closed ceramic tube with a through hole of $200\mu m$ in diameter. Both the XUV and IR pulse are directed through this hole. Within the target cell is a T-shaped outlet connection to the through hole, which allows for some

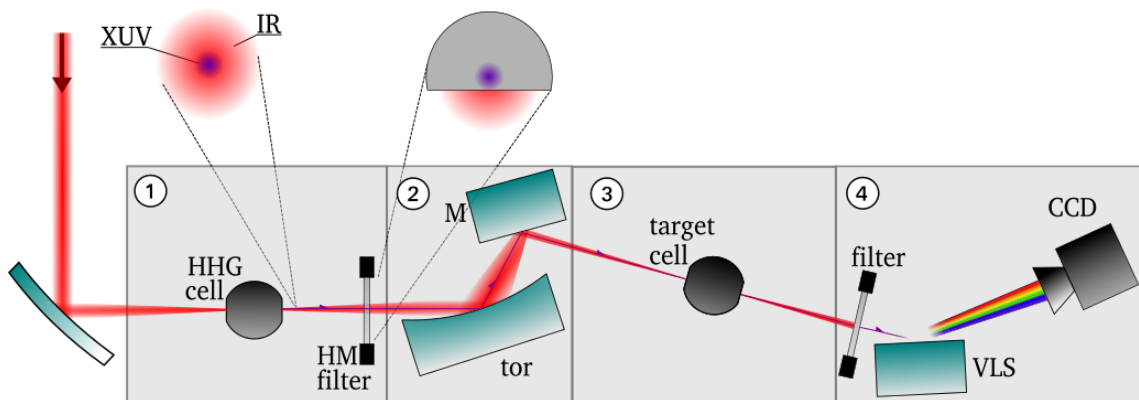


Figure 3.4: Simplified model of the *beamline* before the modifications. ① HHG-chamber; ② mirror-chamber; ③ target-chamber; ④ filters and spectrometer.

gas flow so that a constant pressure within the cell is assured. The target cell is movable in all three spatial dimensions to enable driving it into the common focus of the beams. It is more practical to move the cell into the beampath rather than fixing the target and adjusting the beam-position and -angle. This is because the beampath is fixed in position due to its coupling into the spectrometer within the next experimental section.

At the far end of the beamline is the spectrometer setup, which contains a *Variable Line Space grating* (VLS) to diffract the XUV pulse in its spectral components onto a camera. The camera is a *Princeton Instruments PIXIS CCD camera* (CCD), which allows for the spectroscopy of the XUV pulse after the interaction with the target gas. As the IR light is very intense leaving the XUV light non-detectable, a thin (200-400 μm) zircon filter is placed in front of it, through which XUV beams can pass with attenuated intensity whilst the IR beam is blocked completely.

3.4 Modifications to the Beamline

This chapter describes the planned modifications of the beamline setup to achieve a higher intensity of the IR pulse at the focal plane within the target gas. This can be achieved by redirecting the IR beam coming from the HCF partly. One part of the beam is still used to drive the HHG process. The other is redirected towards the external coupling beampath, which is the main modification to the current setup and will be introduced in the following. Its main parts are the planned installation of a *Time Delay Stage* (TDS), the coupling of the IR beam into the vacuum chamber, its focusing by an *Off-Axis Parabolic mirror* (OAP) movable in all 3 dimensions with the help of motorized stages and its coupling out by another

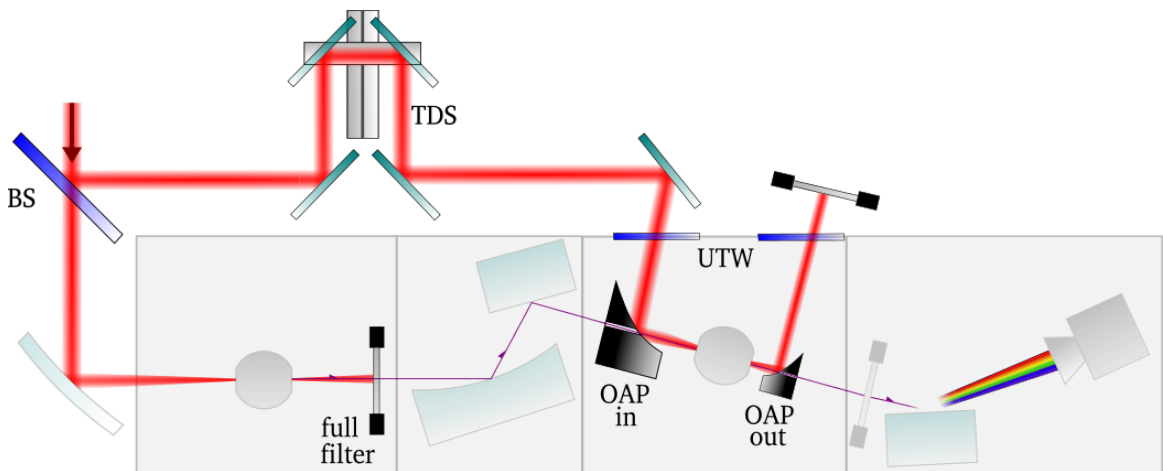


Figure 3.5: Simplified illustration of the *Beamline* after the modifications. The non-greyed parts are the components planned within this thesis project and are explained in more detail within the body text.

OAP. These modifications are shown in Figure 3.5 and explained in the following.

To gain higher intensities with the IR pulse, the approach within this thesis project is to decrease the focal distance, leading to a more compact focal spot as described by (2.10). To gain this smaller focal point, an OAP with a focal length of 3" (= 76.2 mm) is placed in the target chamber to focus the IR beam into the center of the target cell. The original beampath of the IR beam needs to be altered as the share of the same beampath of the XUV and the IR pulse complicate their spatial separation to this extent. The IR beam is split into two roughly equally intense beams by a *BeamSplitter* (BS), of which one enters the beamline, as the total beam did before, generating the XUV spectrum with the HHG mechanism. The remaining IR beam, which passes the HHG-gas without interaction, is blocked completely by metal filters, leaving only the XUV pulse for further usage. The other part of the IR beam, which is reflected at the BS, contains the remaining intensity and travels outside of the beamline. Before this beam is coupled into the target chamber, it is time delayed by a TDS which simply elongates the beampath in space by redirecting it using mirrors. This offers the possibility to vary the arrival time of the IR beam at the interaction region within the target cell. The time delay can be set very precisely as well as within a large time range by using a high-precision, long-range motorized stage. After the TDS, the beam is coupled into the vacuum, target chamber passing through an *Ultra-fast Thin Window* (UTW) optimized for low ϕ_{GDD} and thus stretching the pulse temporal duration just slightly. Placed inside the target chamber is the f=3" OAP.

At this point, the IR and XUV beam overlap again spatially, because the OAP redirects and focuses the larger IR beam by 90° into the beampath of the XUV pulse. The OAP focusing properties described in Chapter 2.4 are applicable to the here presented setup. The smaller XUV beam is guided through a central, $\varnothing \sim 3$ mm hole parallel to the OAP's direction of focus. After interacting with the target gas, the IR beam is redirected out of the XUV beam path. This allows for an analysis of the IR beam after the target cell which is crucial to overlap the IR and the XUV pulse in time. The second redirection is done with a second OAP which is smaller in size and has a focal length of just 2" (= 50.8 mm). Both smaller measurements are due to little space between the chamber wall and the target. This second OAP has a similar central hole to allow the XUV pulse passing through the OAP and into the CCD after the VLS grating. The hole in the second OAP will also let through a fraction of the IR beam which will subsequently be blocked by the filters in front of the VLS.

Planning and designing these modifications was part of this thesis' project. A CAD image of the modified set up in the target chamber is shown and briefly explained in the appendix Chapter A.2.

3.5 Intensity Estimation

For gaining a good understanding of the behaviour of the OAP's degrees of freedom with respect to the focus properties, a measurement series was carried out. These measurements based on an alignment laser give a first estimation for the minimal focal spot size, which, together with the measured pulse duration τ_{FWHM} and energy E_{HCF} , is used to estimate the possible peak intensity I_0 of the LE TiSa IR pulse used in the experiment.

For the measurement series a collimated alignment laser with $\lambda = 776$ nm and $\varnothing \sim 15$ mm, which is slightly smaller than the LE TiSa IR, was used to estimate the focus size achievable with the $f = 3''$ in coupling OAP. The test setup is depicted in Figure 3.6. The apertures A_1 and A_2 were used to align and collimate the beam over a distance of around 4 m. This helps to align the OAP perpendicular to the incoming beam, analogue to the alignment within the experiment. The OAP is mounted with a kinematic mount allowing it to rotate around the Y- and Z-axis, the two axis perpendicular to the incoming beam. The focused beam is captured with a camera, which is placed at the focal distance from the given OAP.

The translation of the OAP in the Y and Z direction is done by eye. A plate with the same diameter as the OAP is placed in the mount. The center of the plate is marked and represents the position of the center of the mount in the YZ-plane. With A_1 the beam is clipped to a tiny dot, which can be aligned with the marked center. After swapping the plate with the OAP, its center in the YZ-plane

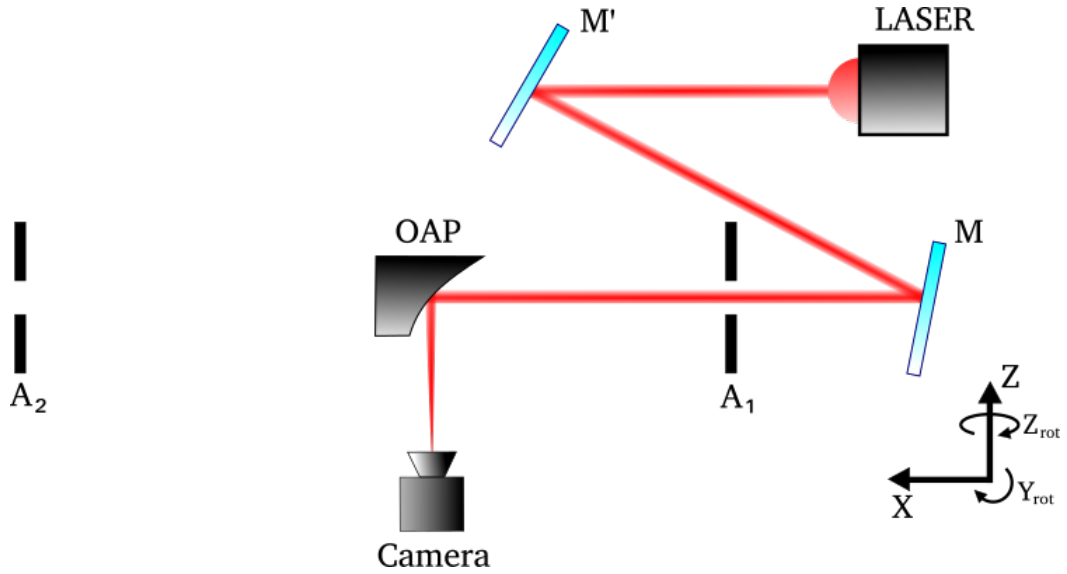


Figure 3.6: Simplified illustration of the 3" OAP test setup seen from above with a weak, 776 nm laser, measuring its focused beam profile.

is aligned to the beam as the mount is designed to spatially overlap its center with the one from the mounted device. Not only the focal spot size was measured with this test setup, but optical aberrations as well. Appendix Chapter A.3 shows several aberrations to the focal image caused by rotational perturbations to the Y- and Z-axis of the optical components within this test setup.

For the case of perfect alignment of the OAP to the predefined beam path, the camera is moved along the Z-axis to find the minimum in focal size. As shown in Figure 3.7, the beam waist follows a hyperbolic profile as expected [13]. The measured beam size minimum is at a FWHM diameter of

$$a_{FWHM} = (8 \pm 4) \mu m , \quad (3.1)$$

whereby the fit-minimum lies even lower. As the collimated LE TiSa beam used in the actual experiment is slightly larger in diameter, its minimal focal waist is expected to be even smaller, making the above given value of a_{FWHM} an upper limit.

With the parameters, E , A and τ , the expected peak intensity I_0 of the TiSa LE IR pulses at the focus position within the target gas of the actual experiment can be estimated via

$$I_0 = \frac{E}{\tau A_f} = \frac{4E}{\tau \pi a^2} . \quad (3.2)$$

E : pulse energy, τ : pulse duration,
 A_f : focal spot area (circular approx.)

With the measured beam diameter $a_{FWHM} = 8 \mu\text{m}$, the pulse duration of $\tau_{FWHM} = 44 \text{ fs}$ and the pulse energy $E_{HCF} = 2.82 \text{ mJ}$, the TiSa IR peak intensity's lower bound can be estimated to

$$I_0 \approx 10^{17} \frac{W}{\text{cm}^2} . \quad (3.3)$$

It should be mentioned that for this estimation, the pulse is assumed to be a square pulse rather than Gaussian shaped in both the temporal as well as the spatial domain, which is good enough for a first estimation of the order of magnitude.

In the following, the achievable IR peak intensity regime of 10^{17} Wcm^{-2} is discussed briefly with respect to known experiments and their IR peak intensity regimes: As shown in [2,3], an IR intensity of $(10^{12} - 10^{13}) \text{ Wcm}^{-2}$ shows a modification in the absorption spectrum of helium with special interest in the $N=2$ series. Thus, higher peak intensities may lead to even stronger modifications and looking at $N \geq 3$ states is the next step in the investigation of helium. These states are reached with the XUV photons and perturbed with the IR field. The

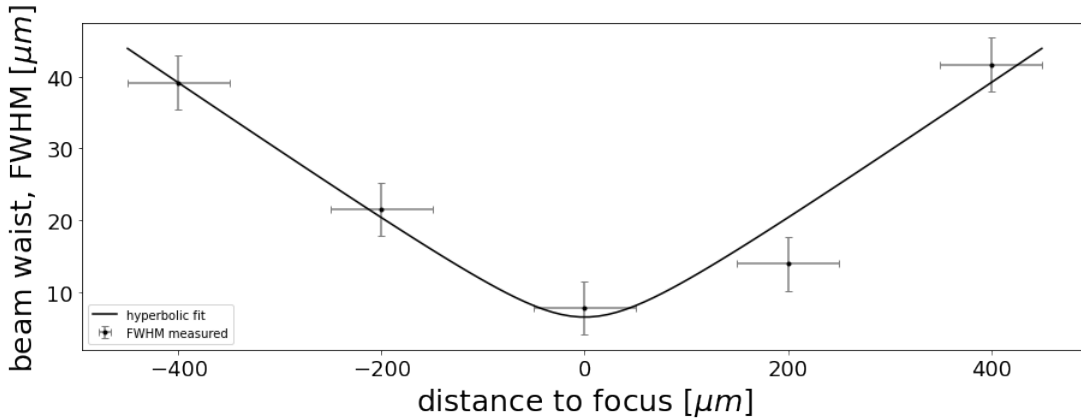


Figure 3.7: Hyperbolic fit for the measured beam waist as a function of the distance z to the focus position. The presented values of the beam waist are the mean over the x- and y-FWHM values for a given distance in z .

actual behaviour of the atoms and the resulting spectroscopic observation depend on the temporal gap between the two pulses. For a preceding XUV pulse, well defined resonances are expected. If the gap between the two pulses decreases, the dynamics within the helium atom are highly speculative. The effect of the perturbing IR on the excited states may vary from ionization to the stabilization of specific states. After the IR has overtaken the XUV, thus preceding it, observing strong-field ionization solely by IR for intensities of $\sim 10^{14} \text{ Wcm}^{-2}$ or higher is likely, as experimental results obtained with 780 nm, 160 fs IR pulses suggest [22]. The single and double ionization would be observed as a decrease in cross section for the energy-resonances above the ionization thresholds.

4 Conclusion

Within this thesis the laser system of the ultra-fast, high intensity laser experimental setup was modified and an external coupling for the dedicated beamline was designed and tested, with the goal to manipulate the electron dynamics of helium to a higher extent. The main enhancements are: 1) the change of the IR pulse's central frequency from the OPA pulse's 1 - 2 μm to the TiSa pulse's ~ 800 nm, 2) short pulse duration of the TiSa IR pulse due to optimized pulse compression and 3) the planned installation of the external coupling using a time delay station (TDS) and an off-axis parabolic mirror (OAP) with a short focal distance as its main components. With the external coupling it is possible to optimize the focus position of the IR beam using a controlling system accessible from outside the vacuum chamber. The time dilation's adjustability is preserved by the TDS. The OAP shrinks down the focal spot size significantly. All three modifications to the experimental setup allow to reach an estimated IR pulse peak intensity in the regime of $10^{17} \text{ W cm}^{-2}$.

With this setup it should be possible to continue the investigation of helium and its interaction with light, in the form of ultra-short and high intense laser pulses. Especially single and probably even double ionization of the neutral helium atom from its ground state should be possible. Further, helium can be exchanged by other atoms or even molecules with rather high ionization potentials. These targets can be affected by the strong, perturbing or ionizing IR, which opens up the field for new possible applications. The dissociation of the O_2 molecule with strong field ionization by the IR pulse and measuring the produced atomic transitions within the XUV spectrum as preparation for an upcoming beam time [23] is one of them.

Further tasks for this project is the generation of high harmonics in the HHG cell with the optimized LE TiSa IR beam followed by first experiments without the external coupling. This defines the status quo and gives the possibility to compare the results of further experiments. Thereafter, the coupling can be installed and optimized for the given setup, which clears the field for first experiments with the modified beamline.

The external coupling can be further improved to different extents. It might be useful to test other splitting ratios but 50/50 given by the beam splitter. The spectroscopic absorption of helium varies with the intensity ratio of the stimulating XUV and perturbing IR.

Another improvement is the motorization of the angular adjustment of the OAPs with priority on the first, coupling OAP. This allows to optimize the size of the focal spot even further. Problematic with the current setup is that the angles only are operable by hand, which binds the fine adjustment to be done before the evacuation of the target chamber. This evacuation process might change the

mechanical orientation slightly, which can not be undone as the chamber is vacuum sealed.

The TDS can be optimized by connecting it with the IR analysis system at the end of the coupling out. Therefore the process of finding the temporal overlap of the XUV and IR pulses can be automatized with a simple algorithm which sets the TDS in the right position for perfect accordance.

Glossary

AS	Absorption Spectroscopy
BS	Beam Splitter
CAD	Computer Aided Design
CCD	Charge-Coupled Device, here: Princeton Instruments PIXIS CCD camera
CEP	Carrier Envelope Phase
CPA	Chirped Pulse Amplifier
cryo SPA	cryogenic Single Pass Amplifier
FWHM	Full Width Half Maximum
FROG	Frequency Resolved Optical Gating
GD	Group Delay
GDD	Group Delay Dispersion
HCF	Hollow Core Fiber
HE	High Energy pulse, coupled into the HE-TOPAS
HE-TOPAS	High Energy Optical Parametric Amplifier for Titanium Sapphire lasers
HHG	High Harmonic Generation
IR	Infra Red
LE	Low Energy pulse
OAP	Off-Axis Parabolic mirror
OD	Optical Density
OPA	Optical Parametric Amplifier
regen	regenerative amplifier
SPA	Single Pass Amplifier
SPM	Self Phase Modulation
SEQ	Schrödinger Equation
TDS	Time Delay Stage
TiSa	Titanium Sapphire
TOD	Third Order Dispersion
VLS	Variable Line Space grating
XUV	eXtreme Ultra Violet

References

- [1] H. Hertz. Ueber einen Einfluss des ultravioletten Lichtes auf die electriche Entladung. *Annalen der Physik*, 267(8):983–1000, 1887.
- [2] C. Ott, A. Kaldun, L. Argenti, et al. Reconstruction and control of a time-dependent two electron wave packet. *Nature*, 516:374–378, 2014.
- [3] Alexander Magunia. Doubly-Excited Helium Strongly Driven with Short and Long Wavelength Pulses. Master’s thesis, Max-Planck-Institut für Kernphysik, 12 2018.
- [4] J.C. Diels and W. Rudolph. *Ultrashort Laser Pulse Phenomena, 2nd Edition*. Academic Press, 2006.
- [5] P. B. Corkum. Plasma perspective on strong field multiphoton ionization. *Phys. Rev. Lett.*, 71:1994–1997, Sep 1993.
- [6] M. Lewenstein, Ph. Balcou, M. Yu. Ivanov, Anne L’Huillier, and P. B. Corkum. Theory of high-harmonic generation by low-frequency laser fields. *Phys. Rev. A*, 49:2117–2132, Mar 1994.
- [7] Wolfgang Demtroeder. *Atoms, Molecules and Photons - An Introduction to Atomic-, Molecular- and Quantum Physics*. Springer-Verlag Berlin, Heidelberg, 2006.
- [8] Jan M Rost, K Schulz, M Domke, and G Kaindl. Resonance parameters of photo doubly excited helium. *Journal of Physics B: Atomic, Molecular and Optical Physics*, 30(21):4663–4694, nov 1997.
- [9] M. Domke, K. Schulz, G. Remmers, G. Kaindl, and D. Wintgen. High-resolution study of $^1P^o$ double-excitation states in helium. *Phys. Rev. A*, 53:1424–1438, Mar 1996.
- [10] David R. Herrick and Oktay Sinanoğlu. Comparison of doubly-excited helium energy levels, isoelectronic series, autoionization lifetimes, and group-theoretical configuration-mixing predictions with large-configuration-interaction calculations and experimental spectra. *Phys. Rev. A*, 11:97–110, Jan 1975.
- [11] A Burgers, D Wintgen, and J M Rest. Highly doubly excited S states of the helium atom. *Journal of Physics B: Atomic, Molecular and Optical Physics*, 28(15):3163–3183, aug 1995.

-
- [12] I Sanchez, H Bachau, and E Cormier. Theory of two-photon spectroscopy of autoionizing states in helium and beryllium. *Journal of Physics B: Atomic, Molecular and Optical Physics*, 28(12):2367–2384, jun 1995.
- [13] Stefan Roth and Achim Stahl. *Optik*. Springer Spektrum Berlin, Heidelberg, 2019.
- [14] Mette B. Gaarde, Christian Buth, Jennifer L. Tate, and Kenneth J. Schafer. Transient absorption and reshaping of ultrafast XUV light by laser-dressed helium. *Physical Review A*, 83(1), Jan 2011.
- [15] Thomas Ding. *Quantum dynamics in weak and strong fields measured by XUV nonlinear spectroscopy*. PhD thesis, Ruperto-Carola-University of Heidelberg, Germany, 2018.
- [16] Marc Anton Alexander Rebholz. *All-XUV pump-probe transient absorption spectroscopy on the dissociation dynamics of small molecules*. PhD thesis, Ruperto-Carola-University of Heidelberg, Germany, 2020.
- [17] Lennart Aufleger. Measurement of electron dynamics in atoms and molecules with intense XUV FEL radiation. Master’s thesis, Max-Planck-Institut für Kernphysik, Germany, 2016.
- [18] Stefano Amberg. Setup and characterization of a hollow core fiber waveguide for transient absorption experiments with short wavelength infrared pulses. Master’s thesis, Max-Planck-Institut für Kernphysik, 2019.
- [19] G. New. *Introduction to Nonlinear Optics*. Cambridge University Press, 2011.
- [20] R.W. Boyd. *Nonlinear Optics*. Elsevier, Ottawa, Canada, 2020.
- [21] JS Robinson, CA Haworth, H Teng, RA Smith, JP Marangos, and JWG Tisch. The generation of intense, transform-limited laser pulses with tunable duration from 6 to 30 fs in a differentially pumped hollow fiber. *Applied Physics B-Lasers and Optics*, 85:525–529, 2006.
- [22] B. Walker, B. Sheehy, L. F. DiMauro, P. Agostini, K. J. Schafer, and K. C. Kulander. Precision Measurement of Strong Field Double Ionization of Helium. *Phys. Rev. Lett.*, 73:1227–1230, 1994.
- [23] A.Magunia, C.Ott and T.Pfeifer and others. FEL-pump-HHG-probe transient absorption spectroscopy on O2, 4 2020.

Appendix

A.1 Doubly Excited States of the Helium Atom

Table A.1.1: Several states lying between the $N=2$ and 3 thresholds. Given are their energy position E compared to the ground state and their spectral width Γ . e-x indicates $\cdot 10^{-x}$. Data is obtained from [8,11,12]. The states are given in the $(K, T)n$ stark quantum number notation.

Group	(K,T)	n	E [eV]	Γ [eV]	Group	(K,T)	n	E [eV]	Γ [eV]	
$^1P^o$	(1,1)	3	69.9	1.90e-01	(2,0)	3	69.42	4.08e-02		
		4	71.65	7.85e-02		4	71.38	2.04e-02		
		5	72.21	3.52e-02		5	72.06	9.49e-03		
		6	72.47	2.07e-02		6	72.39	4.88e-03		
		7	72.62	1.33e-02		7	72.74	2.77e-03		
		8	72.72	8.69e-03		8	72.68	1.70e-03		
		9	72.78	5.92e-03		9	72.75	1.12e-03		
		10	72.82	4.19e-03		10	72.8	7.80e-04		
		11	72.85	3.04e-03		11	72.84	5.64e-04		
						12	72.86	4.12e-04		
		(-1,1)	3	71.34		3.96e-02	(0,0)	3	70.4	9.03e-02
			4	72.18		1.41e-02		4	71.86	3.28e-02
			5	72.47	6.06e-03	5		72.32	1.53e-02	
			6	72.62	2.60e-03	6		72.54	8.63e-03	
			7	72.72	1.53e-03	7		72.66	5.32e-03	
			8	72.78	1.01e-03	8		72.74	3.50e-03	
			9	72.82	7.10e-04	9		72.79	2.42e-03	
			10	72.85	5.15e-04	10		72.83	1.75e-03	
					11	72.86		4.85e-04		
					10	72.86		9.27e-05		
		(2,0)	4	71.25	9.24e-04	(-2,0)	3	72.03	2.86e-04	
			5	72.03	5.97e-04		4	72.38	5.80e-04	
		6	72.38	3.56e-04	5		72.57	4.62e-04		
		7	72.57	2.20e-04	6		72.68	3.35e-04		
		8	72.68	1.43e-04	7		72.75	2.39e-04		
		9	72.75	9.77e-05	8		72.8	1.69e-04		
		10	72.8	6.93e-05	9		72.84	1.23e-04		
		11	72.84	4.34e-05	10		72.86	9.27e-05		
	(0,0)	4	71.75	6.15e-04	$^1D^e$	(2,0)	-	69.71	4.16e+00	
		5	72.27	2.91e-04		(0,2)	-	70.49	3.48e+00	
		6	72.52	1.63e-04		(0,0)	-	71.22	1.15e+00	
		7	72.65	1.00e-04		(2,0)	-	71.53	1.89e+00	
		8	72.73	6.58e-05		(1,1)	-	71.56	2.24e-02	
		9	72.79	4.55e-05		(0,2)	-	71.9	1.18e+00	
		10	72.83	3.28e-05		(0,0)	-	72.12	3.10e-01	
						(2,0)	-	72.14	9.34e-01	
						(1,1)	-	72.18	1.74e-02	
						(-1,1)	-	72.25	3.57e-03	
	(-2,0)	4	72.35	3.69e-06						
		5	72.55	5.75e-06						
		6	72.67	5.53e-06						
		7	72.75	4.66e-06						
		8	72.8	3.74e-06						
		9	72.83	2.98e-06						

A.2 CAD Image

Figure A.2.1 shows a CAD image of the planned modifications within the target chamber. The turquoise parts are the mechanical parts newly introduced. Both OAPs are mounted on stages allowing motorized movement in all three spatial dimensions as well as manual rotation around the Y- and Z-axis. The flanges are sealed with 3 mm thin, low GDD windows.

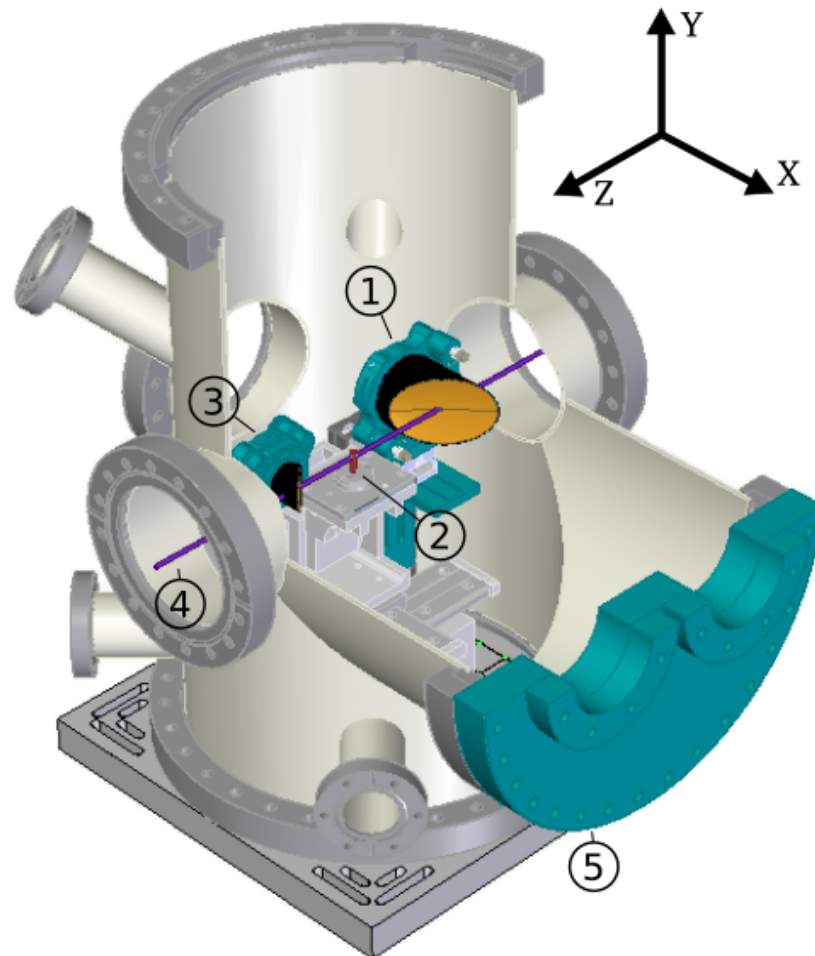


Figure A.2.1: CAD Image of the *Target Chamber* after the planned modification cut open. ① OAP for coupling the IR into the XUV path; ② Target Cell; ③ OAP for coupling the IR out of the XUV path; ④ XUV path; ⑤ flange with coupling windows for the IR beam.

A.3 OAP - Test Measurement Series

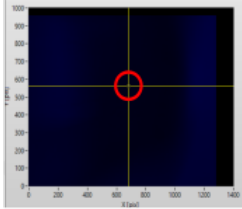
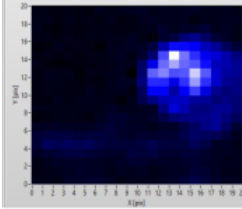
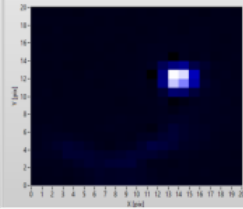
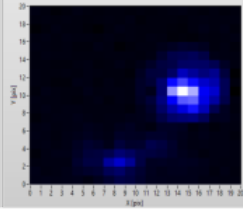
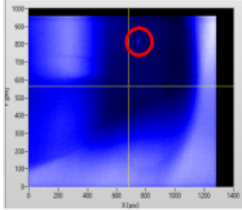
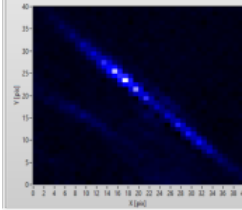
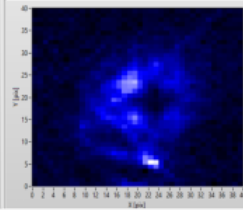
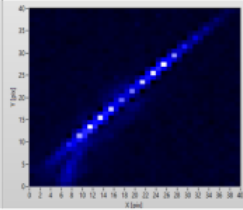
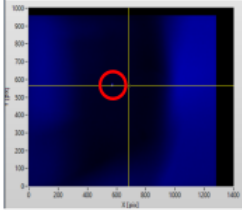
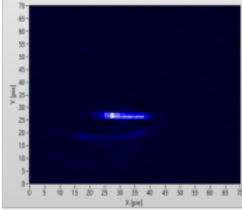
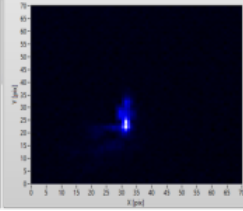
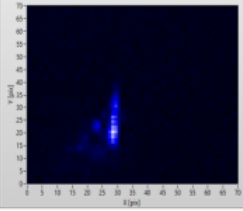
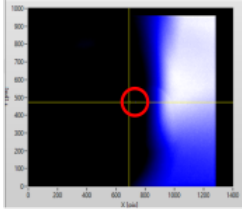
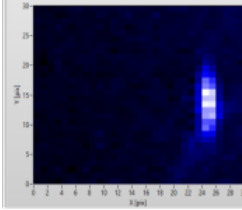
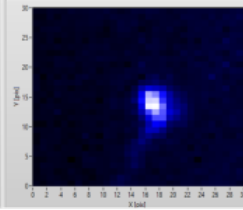
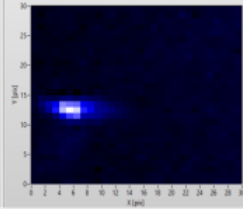
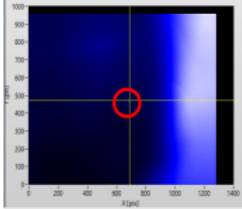
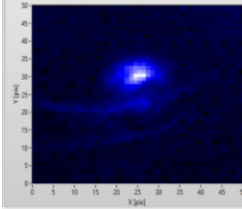
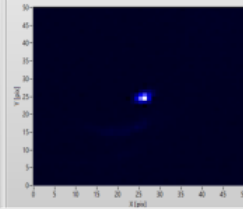
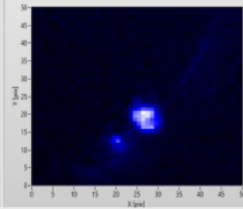
DESCRIPTION	FULL IMAGE	ZOOM IN: characterization of beam profile		
Perfect alignment, minimal focus size.				
		$f - 0.2 \text{ mm}$	f	$f + 0.2 \text{ mm}$
OAP misaligned with Z-rotation. Astigmatism occurs in form of 45° tilted strips out of focus.				
		$f - 0.6 \text{ mm}$	f	$f + 0.6 \text{ mm}$
OAP misaligned with Y-rotation. Astigmatism occurs in form of strips out of focus.				
		$f - 0.4 \text{ mm}$	f	$f + 0.2 \text{ mm}$
Misalignment of incoming beam angle and position with Y-rotation at M, correction with OAP Y-rotation. Astigmatism occurs in form of strips out of focus.				
		$f - 0.2 \text{ mm}$	f	$f + 0.2 \text{ mm}$
Misalignment of incoming beam angle and position with Z-rotation at M, correction with OAP Z-rotation.				
		$f - 0.2 \text{ mm}$	f	$f + 0.2 \text{ mm}$

Table A.3.1: Focus distortion due to different perturbations of an OAP and the incident beam. f is the focal distance of the OAP. Here $f = 3''$ from the center of the OAP. The image axes are given in camera pixels with $1px = 3.75\mu m$. The images are captured with the test setup depicted in Figure 3.6.

Acknowledgment


Zuletzt möchte ich noch einige Worte des Dankes äußern. Wissenschaftliche Projekte in der heutigen Zeit sind schon lange keine Projekte des Einzelnen mehr. Die Tiefe, in der wir Antworten suchen und die damit einhergehende Komplexität der Sache an sich, lassen dies nur schwer zu. Zudem stehe ich erst am Anfang meiner wissenschaftlichen Ausbildung, was bedeutet, dass es für mich noch viel zu begreifen und zu verinnerlichen gibt. Daher bedanke ich mich bei allen Weggefährten der vergangenen Jahre, die mir, im Kleinen und im Großen, das Verständnis und die Fähigkeiten mitgegeben haben, die es braucht, um an diesem Punkt zu stehen. Und auch bei jenen, die den Weg für den mir gegebenen Stand der Forschung bereitet haben, möchte ich mich bedanken. Mein besonderer Dank, vor allem in Bezug auf diese Arbeit, gilt den folgenden Personen:

Prof. Dr. Thomas Pfeifer danke ich für das Ermöglichen dieser Arbeit in seiner Abteilung *Quantendynamik und -kontrolle* am Max-Planck-Institut für Kernphysik und für die Übernahme des Erstgutachtens. **Priv.-Doz. Dr. Robert Moshhammer** für die Übernahme des Zweitgutachten. **Dr. Christian Ott** möchte ich für das Vertrauen danken, an dem von ihm beaufsichtigten experimentellen Aufbau herumzuschrauben, sowie für die guten Ratschläge, vor allem bezüglich der Durchführung, welche sich ersichtlich aus vielen Jahren an Erfahrung und Verständnis ergeben. Ich danke **Dr. Anne Harth** für das Eröffnen dieses Forschungsgebiet im zweiten Semester mir gegenüber. Auch **Patrick Rupprecht**, welchen ich damals als Kollegen von Anne kennenlernte, möchte ich danken, da er mich seitdem ermutigt hat, früh praktische Erfahrung zu sammeln, was letztlich zu der Position als wissenschaftliche Hilfskraft in seinem Team führte, welche sich wiederum zu dieser Bachelorarbeit entwickelte. Ihm danke ich auch für die praktischen Ratschläge an vielen Stellen während der Konzeptionierung der experimentellen Modifikationen. **Felix Henrich** möchte ich danken, da er mir als vorangegangener Bachelorstudent in diesem Team Unsicherheiten und Unklarheiten nehmen konnte. Bei **Peter Gahn** möchte ich mich für die Ratschläge bezüglich der Konstruktion der mechanischen Komponenten bedanken. Und vor allem möchte ich mich bei **Alexander Magunia** bedanken, welcher mich als seinen wissenschaftlichen Helfer aufgenommen hat und von Anfang an stets mit fachlichem sowie persönlichem Rat förderte. Auch danke ich ihm für das sorgfältige Gegenprüfen der Inhalte dieser, meiner ersten wissenschaftlichen Arbeit und für jeden Kniff den er mir gezeigt hat, um im Labor gewissenhaft arbeiten zu können.

Erklärung:

Ich versichere, dass ich diese Arbeit selbstständig verfasst habe und keine anderen als die angegebenen Quellen und Hilfsmittel benutzt habe.

Heidelberg, den 16.04.2021



.....

(Lukas Röhrich)